This article has been accepted for publication in a future issue of this journal, but has not been fully edited. Content may change prior to final publication. Citation information: DOI 10.1109/TBME.2021.3120929, IEEE Transactions on Biomedical Engineering

Sensitivity Analysis Highlights the Importance of Accurate Head Models for Electrical Impedance Tomography Monitoring of Intracerebral Hemorrhagic Stroke

Antti Paldanius, Bachir Dekdouk, Jussi Toivanen, Ville Kolehmainen and Jari Hyttinen

***Abstract*—Objective: Electrical impedance tomography (EIT) has been proposed as a novel tool for diagnosing stroke. However, so far, the clinical feasibility is unresolved. In this study, we aim to investigate the need for accurate head modeling in EIT and how the inhomogeneities of the head contribute to the EIT measurement and affect its feasibility in monitoring the progression of a hemorrhagic stroke. Methods: We compared anatomically detailed six- and three-layer finite element models of a human head and computed the resulting scalp electrode potentials and the lead fields of selected electrode configurations. We visualized the resulting EIT measurement sensitivity distributions, computed the scalp electrode potentials, and examined the inverse imaging with selected cases. The effect of accurate tissue geometry and conductivity values on the EIT measurement is assessed with multiple different hemorrhagic perturbation locations and sizes. Results: Our results show that accurate tissue geometries and conductivity values inside the cranial cavity, especially the highly conductive cerebral spinal fluid, significantly affect EIT measurement sensitivity distribution and measured potentials. Conclusions: We can conclude that the three-layer head models commonly used in EIT literature cannot depict the current paths correctly in the head. Thus, our study highlights the need to consider the detailed geometry of the cerebrospinal fluid (CSF) in EIT. Significance: The results clearly show that the CSF should be considered in the head EIT calculations.**

***Index Terms*—electrical impedance tomography, lead field theory, sensitivity distribution, stroke imaging, stroke monitoring**

I. Introduction

Stroke is the second leading cause of death worldwide, causing 5.5 million deaths annually. Up to 50% of stroke survivors are permanently disabled. The public health burden of stroke is expected to increase as the population ages, especially in developing countries [1]. The diagnosis of stroke and monitoring of stroke are both areas where novel methods are needed. Here we discuss the challenges of modeling the head as a volume conductor for 3D electrical impedance tomography for monitoring of hemorrhagic stroke.

There are two main types of stroke, ischemic and hemorrhagic, with generally 80% of the cases being ischemic and the remaining being hemorrhagic [1]. While hemorrhagic stroke represents only a minority of the cases, it carries significantly higher mortality rates than ischemic stroke. Repeated bleeding and hematoma expansion are common complications resulting in poor outcomes and increased mortality. [2], [3]

Computed tomography (CT) is the preferred way of diagnosing and monitoring intracerebral hemorrhage (ICH). Magnetic resonance imaging (MRI) can also be used, but CT is generally more available in emergency departments. Both CT and MRI are not suitable for continuous monitoring of the patient. If the patient's condition changes, the only way to see if the ICH is progressing is to transport the patient from the intensive care unit to the imaging facilities for another set of CT or MR images. Increased intracranial pressure (ICP) may indicate intraventricular hemorrhage or mass effect from a large hematoma or edema; however, it cannot provide information on the causes. [3], [4]

Electrical impedance tomography (EIT) is a promising imaging technique that has the potential to provide a solution for continuous bedside monitoring for patients suffering from ICH. While EIT doesn't offer the spatial resolution of CT or MRI, it has a high temporal resolution, and the EIT measurement setups are generally portable and low-cost [5]. Thus, they could enable continuous assessment of the medical condition [6]. In EIT, a priori information of the conductivity distribution of the measured volume can be used to constrain the inverse solution [7]. In monitoring ICH with EIT, this would be patient-specific a priori information about the patient head anatomy based on the routine CT/MRI data acquired to diagnose the stroke.

Previous EIT brain imaging research targets have included epilepsy [8], differentiation between intracerebral hemorrhage (ICH) and ischemia [9], [10], monitoring progression of a hemorrhagic stroke [11], or other conditions which may alter the impedance of tissues inside the cranial cavity [12]. While computational and phantom models have provided promising results, there has been only one clinical study on the feasibility of EIT in delivering diagnostic information for differentiation of different pathologies such as ischemic and hemorrhagic

Submission date: February 3rd, 2021. This work was funded by Jane and Aatos Erkko foundation Grant on "EIT – a novel method for improved diagnostics of stroke".

Antti Paldanius (corresponding author) is with the Faculty of Medicine and Health Technology, Tampere University, 33720 Tampere, Finland (e-mail: antti.paldanius@tuni.fi)

Jari Hyttinen and Bachir Dekdouk are with the Faculty of Medicine and Health Technology, Tampere University

Ville Kolehmainen and Jussi Toivanen are with the Department of Applied Physics, University of Eastern Finland

This article has been accepted for publication in a future issue of this journal, but has not been fully edited. Content may change prior to final publication. Citation information: DOI 10.1109/TBME.2021.3120929, IEEE Transactions on Biomedical Engineering

stroke and tumors [12], and it had negative findings. Differentiation of pathologies is a more challenging application than monitoring of ICH, which is our primary interest. In this clinical study, a five-layer (scalp, skull, cerebrospinal fluid, grey matter, and white matter) finite element (FE) mesh with simplified geometry layers without anatomical details such as the sulci of the brain was used for both measurement channel sensitivity analysis and EIT reconstruction. This underlines the need to study the possible ways to improve the computational models to match their real-life counterparts more closely.

Computational modeling of EIT provides a way to assess its capabilities in detecting bioimpedance changes or to design the measurement configurations [5]. When modeling the EIT measurements, we can either simulate the measurements directly and obtain electrode potentials or compute the difference in measured voltages caused by the perturbation in question. Alternatively, models can be used to compute lead fields to visualize and assess the sensitivity of the measurements [5]. The lead field theory [13], [14] provides a powerful tool to visualize and determine the sensitivity distribution of impedance measurement and its sensitivity to changes in electrical conductivity in any region of the measured domain [5]. Lead field theory has been proposed as a tool for designing impedance cardiography [15] and micro-electrode arrays for bioimpedance measurements [16] but is rarely mentioned with brain EIT. Kauppinen et al. used the lead field concept for visualizing the head EIT measurement and the current injection and voltage measurement patterns in a 2D slice [5]. Seoane et al. used a 3D head model but only calculated sensitivity for the current injecting electrodes [17].

Overall, in most of the previous EIT head modeling studies, relatively simple models of the head and its inhomogeneities were used; a three-layer model with brain, skull, and brain compartments or otherwise geometrically simplified model has been the usual approach [10], [18]–[22], though lately some higher detail models similar to the one presented in this article have been developed. However, they were primarily used for a software demonstration, and they did not use frequency-dependent material properties [23]. Also, water tank experiments often replicate the three-layer model setup with skull separating the scalp and intracranial cavity, which has homogeneous conductivity [24], [25], or use a single compartment [26], [27].

In a recent study, Jehl et al. [28] explored the effect of patient-specific accurate tissue modeling on stroke detection using EIT time-difference imaging. Their seven-layer models included scalp, skull, CSF, white matter, grey matter, diploë, and sagittal sinus and air, closely resembling the model used in this paper. While the utilization of anatomically structured meshes in the linear difference reconstruction didn't improve the actual stroke detection, it was discovered they resulted in better image quality. From our perspective, this would be of interest when monitoring the progression of an existing hemorrhagic stroke as it could make smaller changes detectable.

In this computer modeling study, we aim to study the capability of 3D EIT to detect intracerebral hemorrhage in the brain and assess the importance of the anatomical details, especially the cerebrospinal fluid, on EIT measurements. We use the finite element method (FEM) to model the human head accurately and use lead fields to visualize the sensitivity distributions of 3D EIT measurements. We also compute the measured EIT voltages to simulate the impedance measurement and assess their detectability. We compare these in a simplified anatomical three-layer model and anatomically accurate six-layered model with detailed CSF and brain geometry to evaluate the effect of the anatomical details and especially the role of CSF in EIT. We also examine how the size and depth of the ICH perturbation affect the sensitivities and measured voltages.

Based on our results, we will discuss the need for accurate modeling and the feasibility of impedance measurement for monitoring a hemorrhagic stroke. We mainly approach the problem from the forward problem perspective to omit the possible bias of different inverse EIT algorithms. However, we provide an example of how the complexity of the model affects inverse imaging using commonly used total variation regularized nonlinear least-squares reconstructions.

II. Materials and Methods

A. Lead field theory

Lead field theory states that the measured impedance Z in the measured volume can be described by

$$Z = \int_v \frac{1}{\sigma} \bar{J}_{LE} \cdot \bar{J}_{LI} \, dv \tag{1}$$

where σ is the electrical conductance and $\bar{J}_{LE}$ and $\bar{J}_{LI}$ are the current density vector fields, or the lead fields, of the current injection and the voltage measurement leads, respectively [5], [13]. These can be obtained by applying a unit current to both the current injection and voltage measurement electrode pairs. Dot product between $\bar{J}_{LE}$ and $\bar{J}_{LI}$ produces scalar sensitivity field S, which expresses how sensitive the measurement is to changes in conductivity in different regions of the measured volume. The equation for the scalar sensitivity field

$$S = \bar{J}_{LE} \cdot \bar{J}_{LI} \tag{2}$$

was implemented in COMSOL, and the results were visualized on a 2D slice of the 3D head models.

B. Head model and finite element mesh generation

Pre-segmented healthy human head from the Population Head Model repository [29] was used as a basis for the head FE models. These pre-segmented head models contained STL-format surface models of scalp, skull, CSF, grey matter, white matter, cerebellum, and ventricles. Thirty-two electrodes with a diameter of 10 mm were placed on the scalp (Fig. 1). The electrodes were selected from EEG 10-5 system based on recommendations by Goren et al. for EIT measurements [30]. The pre-segmented surfaces were imported into Synopsis ScanIP Simpleware for meshing. A finite element mesh of ~ 2.5 million tetrahedral elements was created. Adaptive meshing was used to mesh regions, such as areas around the electrodes, with higher density to improve the accuracy of the simulations.

This article has been accepted for publication in a future issue of this journal, but has not been fully edited. Content may change prior to final publication. Citation information: DOI 10.1109/TBME.2021.3120929, IEEE Transactions on Biomedical Engineering

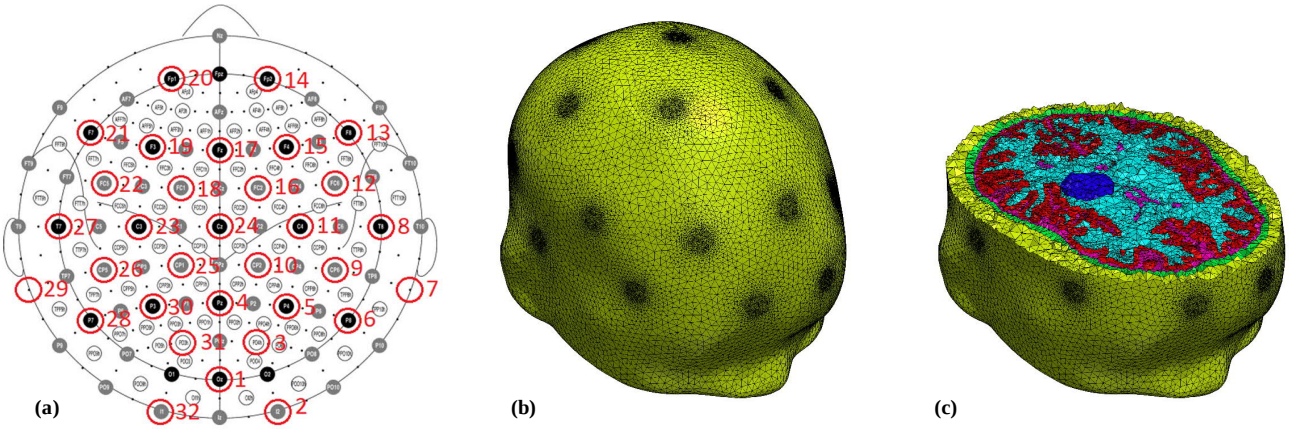

Fig. 1. (a) The 32 electrodes used from the extended 10-5 system are circled in red and numbered. (b) Surface of the finished FE mesh. The electrode locations are meshed with denser mesh. (c) Cross section of the finished FE mesh displaying the different tissue layers and a spherical perturbation inside the brain.

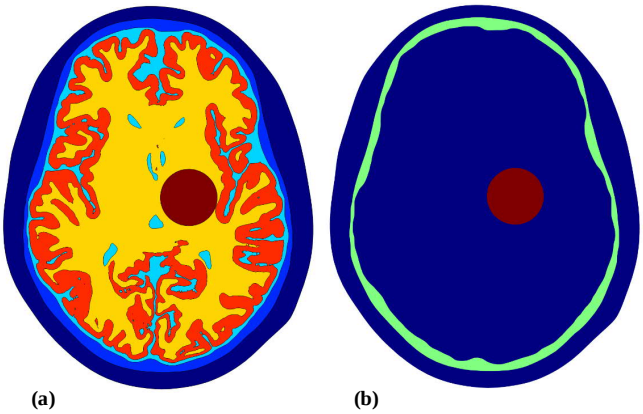

Fig. 2. 2D slices of the 3D head models with different tissue layers visible. (a) The six-layer model and (b) the three-layer model. A spherical 30 mm diameter perturbation has been included in both.

Simple perturbations modeling an ICH were created by creating spherical geometric primitives and inserting them into the pre-segmented head model (Fig. 1 and 2). The default diameter of the perturbation was 30 mm, and the distance to the scalp was 65 mm from the center of the perturbation. This perturbation location was carefully selected, so it would only overlap white matter in the six-layer model. One perturbation series was created where the perturbation location was the same as the default, but the diameter was grown from 10 mm to 30 mm in 5 mm steps. FE meshes were also created for different perturbation locations where the perturbation was moved in 10 mm steps towards the temporal region of the brain with a maximum displacement of 30 mm from its original location in the basal ganglia region. In the six-layer model, moving the perturbation caused some overlapping of the perturbation and grey matter and CSF layers.

C. EIT forward model setup in COMSOL

The EIT measurements were simulated in COMSOL Multiphysics 5.5. The electric currents physics interface from the AC/DC-module was used as it supports alternating current injections and the use of frequency-dependent material properties. The frequency-dependent material properties for different tissue layers (Table I) were obtained from Gabriel's extensive work on the dielectric properties of tissues [31]. The tissue layers included in the six-layer model are the scalp, skull, CSF (including ventricles), grey matter, white matter, and cerebellum. The three- and six-layer models use the same FE meshes to avoid potential discretization-related differences in the results. The three-layer model was built by giving each tissue domain inside the cranial cavity the same conductivity as the scalp. So, the finalized three-layer model comprised of the scalp, skull, and homogeneous mass inside the cranial cavity. When the perturbation is present in the model, it is modeled with the material properties of blood using the Material Switch function of COMSOL. It is worth noting that the relative conductivity change in the six-layer model with respect to the surrounding tissue is much larger when the perturbation is present compared to the three-layer model. In the three-layer model, the scalp and the contents of the cranial cavity have a conductivity of 0.32 – 0.36 S/m depending on the frequency used. The white matter present in the six-layer model has a much lower conductivity of 0.06 – 0.08 S/m, while the ICH lesion has a conductivity of 0.7 S/m. So, in the three-layer model, the conductivity difference of the lesion and background is just over 2:1, while in the six-layer model, the difference is approximately 10:1. Complete electrode model (CEM) has become the standard for accurate modeling of electrode measurements in EIT [32]. For the electrode model, COMSOL implementation of CEM by Fouchard [33] was used. This CEM implementation was benchmarked against EIDORS in the paper [33]. This CEM implementation couples both the contact impedance and the current injection into a single Neumann boundary condition,

$$-n \cdot j = \frac{1}{z_e \|E_e\|}\left(\int_{E_e} v \, d\Gamma + z_e i_e - \|E_e\| v\right) \tag{3}$$

where $n \cdot j$ is the normal current density, z_e is the contact impedance, i_e is the injected current, $\|E_e\|$ is the surface area of the electrode, and v is the electric potential. The electrodes defined in the imported FE mesh were numbered from 1 to 32 (Fig. 1). The electrodes were paired in 1-2, 2-3, …, 32-1 order to facilitate the calculation of differential voltages.

COMSOL with MATLAB LiveLink interface was used to automate the setup of boundary conditions and probes,

This article has been accepted for publication in a future issue of this journal, but has not been fully edited. Content may change prior to final publication. Citation information: DOI 10.1109/TBME.2021.3120929, IEEE Transactions on Biomedical Engineering

variables, material properties, current injection patterns, and parts of the post-processing pipeline.

We selected five different current injection patterns with 1 mA alternating current to visualize the lead fields and assess the measured voltages of different impedance measurement configurations. Electrode pairs 1-17, 2-15, 8-27, 6-14 and 8-13 were chosen, as they provide visualization of sensitivity patterns for adjacent (electrode pairs 6-14 and 8-13), opposite (electrode pairs 1-17 and 2-15) and cross (electrode pairs 1-17 and 8-27) measurement patterns.

The current injections were simulated at 1000, 10000, and 100000 Hz frequencies, and the tissue impedances were changed accordingly (Table I). While the complete electrode model used permits the use of complex impedance for the electrodes, the contact impedance of the electrodes was set to have a real value of 2000 Ω, which is within the acceptable range for Ag/AgCl scalp electrodes [34]. COMSOL's built-in iterative BiCGSTAB solver was used for solving the impedance measurement simulation.

The 3D electric field resulting from the applied current from the selected electrodes was simulated. The results were used to calculate lead fields in the 3D head volume and the scalp potentials to simulate the sensitivity distribution and EIT voltage measurements, respectively. One pass of current injection simulations with a single perturbation type took approximately 2 hours with a PC fitted with Intel Core i7-8700 hexacore CPU and 64GB of RAM.

Simulations were completed with the six- and three-layer head models with four different perturbation locations and five sizes. Visualizations of the sensitivity distributions were produced for both types of models with multiple different perturbation locations. All in all, the study included 165 current injection simulations.

Additionally, full EIT measurement simulations with 32 independent current injection patterns were performed with the three- and six-layer models for an EIT reconstruction example. Four sets of full EIT solutions were computed; one set of simulations with both models set to healthy configuration (no perturbation) and one set with both models having the 30 mm perturbation in the basal ganglia region, typical location of ICH originating from middle cerebral artery bleeding.

D. Post-processing the simulation results

COMSOL's default implementation for obtaining current densities was used to determine the lead fields of the current injecting and measuring electrode pairs. The current density vector lead fields of the current injecting and voltage measurement electrodes were visualized on top of the current density images with a magnitude-controlled distribution of current flow lines. The dot product of these lead fields produces the sensitivity distribution of the current feeding and voltage measurement configuration (Equation 2). This dot product was calculated within COMSOL.

A 2D axial slice (Fig. 2) of the 3D head model was defined for visualization purposes. Current densities and sensitivity distributions of different current injection patterns were visualized on this plane. One 3D sensitivity distribution image was included as an example (Fig. 6).

The differential voltage between the electrode pairs was calculated in COMSOL post-processing. Differential voltage was chosen as a measurement method to eliminate the need for a common electrode [35].

The potential difference on the entire surface of the scalp between a case with a perturbation and without a perturbation was calculated for three current injections using electrode pairs 1-17, 8-13, and 8-27. Visualization of the potential difference was rendered to show how the presence of the perturbation affects the potential distribution on the entire scalp with the above-mentioned current injection patterns.

The impedance measurements on the electrode potentials were calculated using boundary probes on the electrode boundaries of the model and solving

$$v_e = \frac{1}{||E_e||}\int_{E_e} v\, d\Gamma + z_e i_e \qquad (4)$$

for each electrode boundary. Differential voltages between electrode pairs were calculated.

The effect of the size and location of the perturbation on the simulated differential voltages was calculated in Excel by calculating the measurement difference between a healthy head and model with a perturbation and its median difference of each measurement electrode pair in all current injection patterns and frequencies. In addition, the median percentage change between the no-perturbation and perturbation situations was also calculated.

All lead field and sensitivity distribution visualizations were performed on 100 kHz frequency as for visualization purposes, there was very little difference in the sensitivity distributions between the frequencies simulated in this study.

E. Image reconstruction

The simulated full EIT measurement datasets were used to compare the effect of the model for data simulation on reconstructed images. Noisy realizations of the simulated measurement data were obtained by adding Gaussian zero-mean random noise with a standard deviation equal to 0.01 % of the maximum amplitude of the voltages to the simulated noiseless measurements. The standard deviation of the noise

TABLE I
DIELECTRIC PROPERTIES OF TISSUES

	Scalp		Skull		Cerebrospinal fluid		Cerebellum		White matter		Grey matter		Intracerebral hemorrhage	
f (Hz)	σ (S/m)	ε_r	σ (S/m)	ε_r	σ (S/m)	ε_r	σ (S/m)	ε_r	σ (S/m)	ε_r	σ (S/m)	ε_r	σ (S/m)	ε_r
1000	0.32	434932	0.02	2702	2	109	0.12	164358	0.06	69810	0.10	164062	0.70	5259
10000	0.34	25908	0.02	522	2	109	0.13	22535	0.07	12467	0.11	22240	0.70	5248
100000	0.36	8089	0.02	228	2	109	0.15	3515	0.08	2107	0.13	3221	0.70	5120

Material properties used in this study. Each tissue had conductivity (σ) and relative permittivity (ε_r) defined for every current injection frequency. [28]

This article has been accepted for publication in a future issue of this journal, but has not been fully edited. Content may change prior to final publication. Citation information: DOI 10.1109/TBME.2021.3120929, IEEE Transactions on Biomedical Engineering

was on average 0.14 % of the absolute values of the noiseless voltages. The measurements were simulated using a current frequency of 1 kHz.

Reconstructed images were computed by solving a nonlinear least-squares problem regularized with isotropic smoothed total variation regularization, as in [36], by solving

$$\sigma = \arg\min_{\sigma>0} ||V - U(\sigma)||^2 + TV(\sigma) \quad (5)$$

where V are the measured and $U(\sigma)$ the forward model electrode voltages. The regularization term $TV(\sigma)$ favors reconstructed images with sparse gradients and can be written as [37]

$$TV(\sigma) = \alpha \int_\Omega (||\nabla\sigma||^2 + \beta^2)^{1/2} dx \quad (6)$$

where α is a weight coefficient, $\nabla\sigma$ is the gradient of the conductivity, and β is a small smoothing parameter. A wide range of α and β values were tested, and the value pairs giving the visually best-reconstructed images were chosen for the reconstruction comparison. When using data from the three-layer model α = 0.1 and β = 1e-4 were used and when using data from the six-layer model α = 1 and β = 1e-5 were used.

In the image reconstruction solution, the surface of the head and electrode locations on the skin were assumed known – the image reconstruction model did not utilize any of the anatomical information of the three- or the six-layer models. Instead, the forward solutions and reconstructed images were computed using a non-structured head mesh. A constant initial guess equal to the conductivity of scalp tissue was utilized in iterative Gauss-Newton minimization of the regularized nonlinear least squares functional in (5).

III. Results

A. Visualizations of current density and sensitivity distributions

Fig. 3 displays an example of the resulting current density fields and lead fields from electrode pairs 6-14 and 8-13. The resulting scalar sensitivity field S visualizes the sensitivity distribution of the four-electrode measurement setup. As the current density near the electrodes is orders of magnitude higher

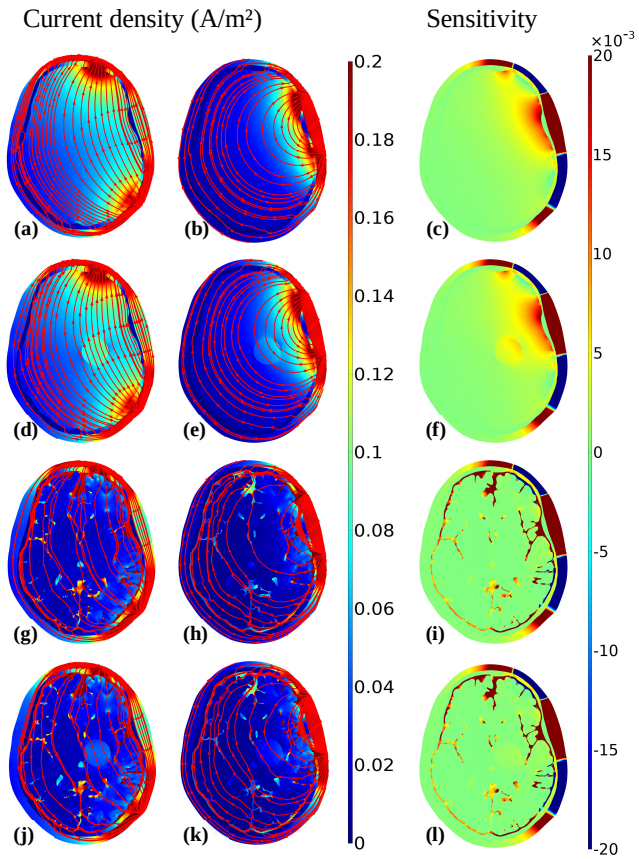

Fig. 3. (a) and (b) display the current density and current density lead fields of electrode pairs 6-14 and 8-13 respectively in the three-layer model. (c) is the resulting sensitivity distribution. (d), (e) and (f) are otherwise the same setup but a 30 mm hemorrhagic perturbation is included in the model. The current densities and lead fields in the six-layer model with current injection pairs 6-14 and 8-13 is displayed in (g) and (h) with the resulting sensitivity distribution in (i). (j), (k) and (l) have the 30 mm hemorrhagic perturbation included.

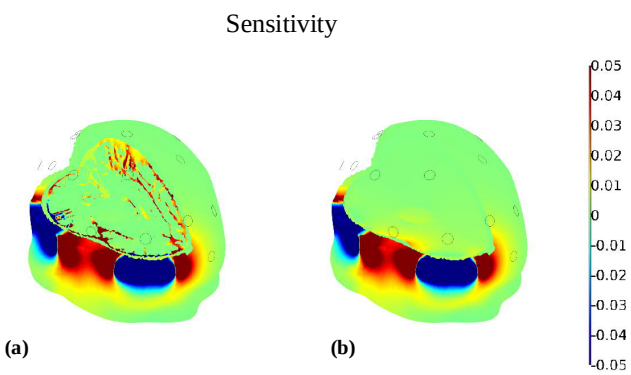

Fig. 4. Examples of 3D sensitivity distributions with adjacent measurement pattern using electrode pairs 6-14 and 8-13. (a) the six-layer model and (b) the three-layer model.

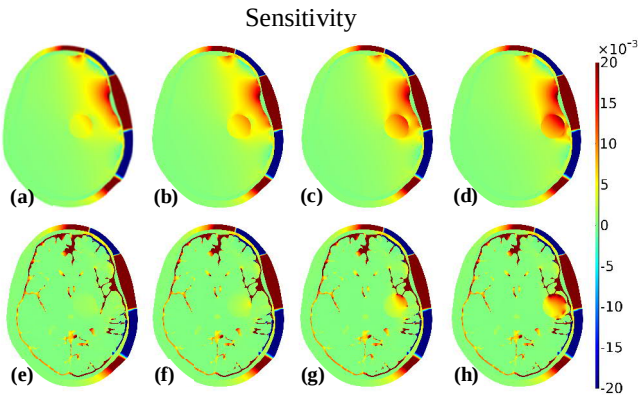

Fig. 5. The 30 mm hemorrhagic perturbation is moved gradually towards the temporal region in 1 cm steps. This alters the sensitivity distribution inside the cranial cavity. Three-layer model is in the top row with (a) being the starting position for the perturbation and in (b), (c) and (d) the perturbation is moved towards the temporal location. (e), (f), (g) and (h) display the same setup with the six-layer model.

This article has been accepted for publication in a future issue of this journal, but has not been fully edited. Content may change prior to final publication. Citation information: DOI 10.1109/TBME.2021.3120929, IEEE Transactions on Biomedical Engineering

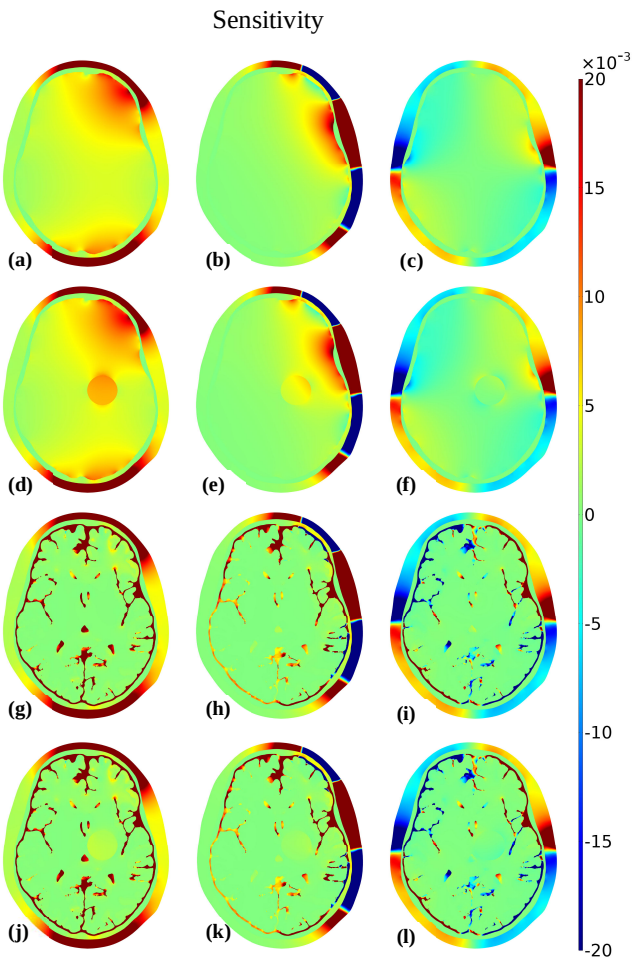

Fig. 6. Sensitivity distributions with three different measurement patterns in the three- and six-layer models both with and without the perturbation. (a), (b) and (c) have the three-layer model without the perturbation with opposite, adjacent and cross measurement patterns respectively. In (d), (e) and (f) a 30 mm hemorrhagic perturbation is added to the model. (g), (h) and (f) display the same measurement patterns in a six-layer model without a perturbation and (j), (k) and (l) with a perturbation.

than inside the cranial cavity, the measurement sensitivity is also relatively high near the electrodes. The sensitivity values were capped in the visualization at 0.02 and -0.02 for the 2D slices and 0.05 to -0.05 for the 3D image as the CSF and the scalp shunt current very effectively (Fig. 3). The sensitivity in the CSF and scalp domains reach significantly higher values than anywhere else in the model.

This current shunting by CSF increases the overall current density and sensitivity inside the cranial cavity in the six-layer model compared to the three-layer model. As the hemorrhagic perturbation also has higher conductivity than the surrounding tissues, it also alters the lead fields and the sensitivity distributions inside the cranial cavity in both three- and six-layer models.

Fig. 4 displays the sensitivity distribution of the four-electrode measurement setup in Fig. 3 in 3D space to further highlight the differences between the three- and six-layer models.

Fig. 6 demonstrates how different measurement and current injection electrode pairs produce different sensitivity distributions inside the cranial cavity and how much the more anatomically accurate six-layer model differs from the three-layer model. The first simulated measurement pattern with electrode pairs 1-17 and 2-15 shows how injecting current through the head and measuring the voltage along the same axis with nearby electrodes provides some sensitivity even in the deepest regions inside the head in the simple three-layer model. In the six-layer model, the CSF effectively shunts the current, and the sensitivity is more distributed around the actual brain tissue. In the middle panel of Fig. 6, the measurement and injecting electrodes are moved to the same side of the head (electrode pairs 6-14 and 8-13), and the images demonstrate how this provides better sensitivity in the temporal region thus on superficial layers of the brain in both the three- and six-layer models. On the right column, the cross-pattern formed by electrode pairs 1-17 and 8-27 results in equal areas of negative and positive sensitivity inside the cranial cavity, and the pattern of sensitivity becomes very complex.

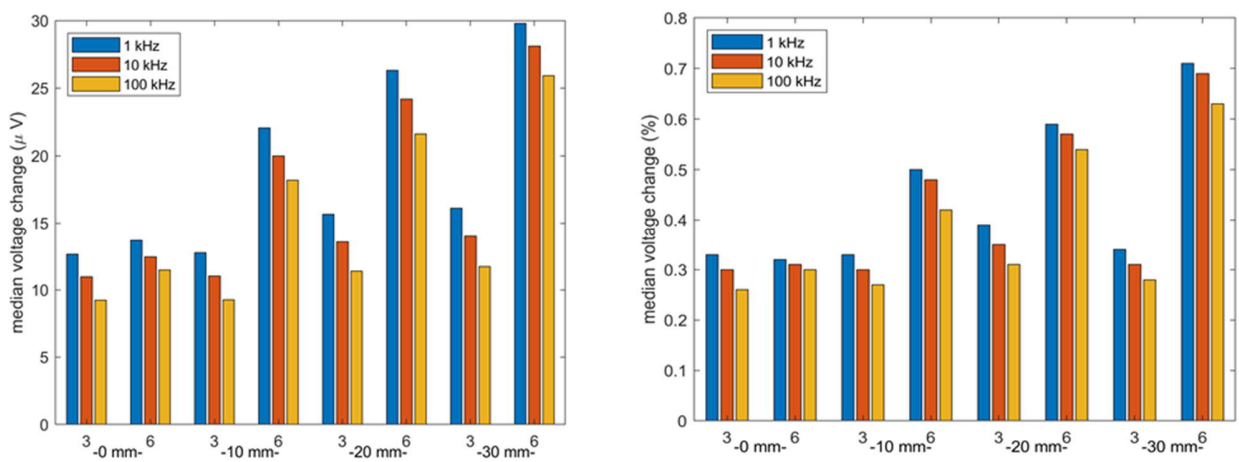

Fig. 7. The perturbation was moved from the basal ganglia region to the temporal region in 10 mm steps in both three- and six-layer models. Five current injections were simulated on 1000, 10000 and 100000 Hz frequencies and the differential voltages between electrodes were recorded. The median voltage change resulting from the perturbation when compared to baseline healthy head model was calculated. On the left chart the median voltage change is presented as an absolute value (μV) and as relative percentage change on the right.

This article has been accepted for publication in a future issue of this journal, but has not been fully edited. Content may change prior to final publication. Citation information: DOI 10.1109/TBME.2021.3120929, IEEE Transactions on Biomedical Engineering

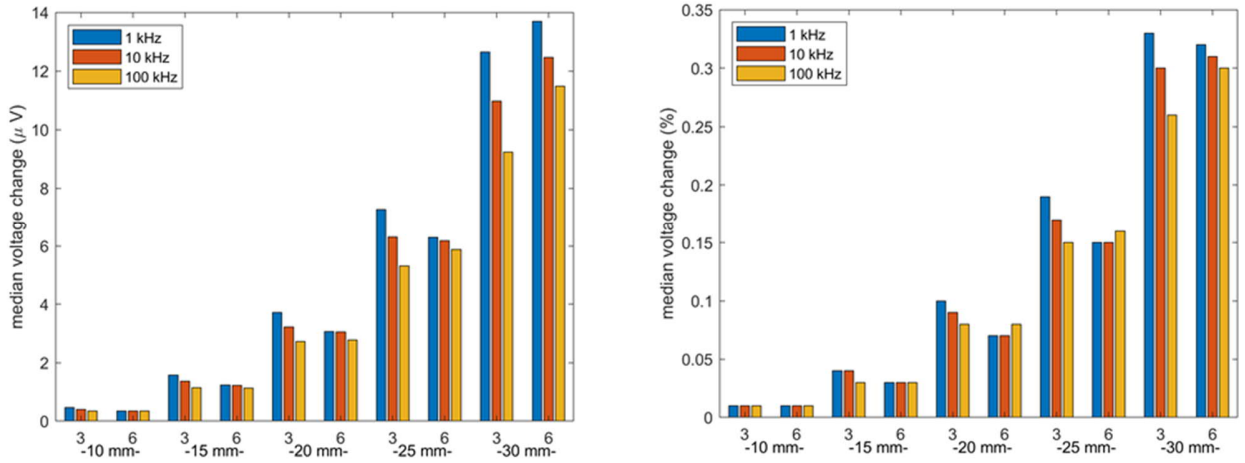

Fig. 8. The perturbation was in the basal ganglia region and its diameter was increased in 0.5 cm steps in both three- and six-layer models. Five current injections were simulated on 1000, 10000 and 100000 Hz frequencies and the differential voltages between electrodes were recorded. The median voltage change resulting from the perturbation when compared to baseline healthy head model was calculated. On the left chart the median voltage change is presented as an absolute value (μV) and as relative percentage change on the right.

Fig. 5 depicts the effect of the perturbation location; even if the measurement and current injection pair stay the same as in Fig. 3, the sensitivity distributions are different due to the different locations of the perturbation. In the three-layer model, the cranial cavity is homogeneous except for the perturbation. It can be observed that moving the perturbation does not significantly affect the sensitivity as in the six-layer model. There is a notable difference in the six-layer model when the perturbation is moved towards the temporal region as the insulating layer of grey and white matter gets smaller, and the perturbation comes closer to the well conductive CSF layer, increasing the current density lead field strength in the area of the perturbation.

B. Contribution of perturbation to the differential voltage measurements

The effect of the location and the perturbation size on the simulated voltage measurement results are presented in Fig. 7 and Fig. 8.

In Fig. 7, the perturbation was located as shown in Fig. 2 in the basal ganglia region, and then it was moved towards the temporal region in 10 mm steps. The median differential voltage change between electrode pairs was calculated in both absolute value and percentage change.

The effect of the perturbation size was also calculated with the perturbation in the same location as in Fig. 2 but now growing progressively from 10 mm to 30 mm diameter in 5 mm steps. These results are presented in Fig. 8. When the perturbation size is reduced to less than 25 mm, its effect on the voltage measurement diminishes quickly on both the three- and six-layer models.

Fig. 10-12 display the differences in the scalp potentials between the healthy head model and a head model with 30 mm hemorrhagic perturbation in the basal ganglia region. These were simulated for both the three- and the six-layer models with opposite, adjacent, and cross current injection patterns. Overall, both the measured voltages in Fig. 7 and Fig. 8 and the scalp potential difference images Fig. 10-12 show that the more complex and anatomically realistic six-layer model differs from the three-layer model. In those cases, the median differential voltages had a difference of 4.6 % between the three- and six-layer models.

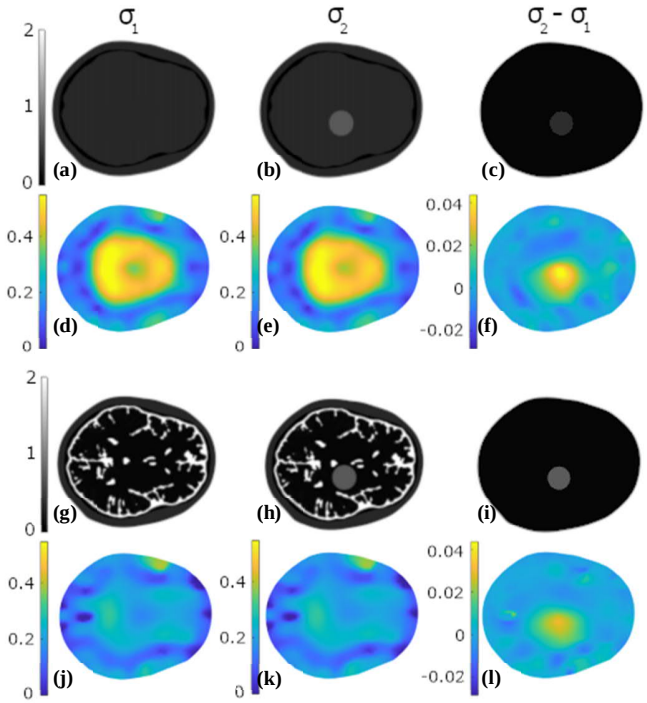

Fig. 9. Comparison of total variation regularized reconstructions computed using measurement data simulated using the 3-layer model (a - f) and the 6-layer model (g-l). The first column (a, d, g, j) shows the "healthy" conductivity σ_1, the second column (b, e, h, k) shows the "stroke" conductivity σ_2 and the third column (c, f, i, l) shows the change in conductivity $\sigma_2 - \sigma_1$ from the "healthy" to the "stroke" conductivity. The first row (a, b, c) and the third row (g, h, i) show the true targets and the second row (d, e, f) and the fourth row (j, k, l) show the reconstructed conductivities. The unit of conductivity is S/m.

This article has been accepted for publication in a future issue of this journal, but has not been fully edited. Content may change prior to final publication. Citation information: DOI 10.1109/TBME.2021.3120929, IEEE Transactions on Biomedical Engineering

C. *Total variation regularized reconstruction*

The reconstructed images are shown in Fig. 9. The top two rows correspond to the 3-layer model (a - f) and the bottom two to the 6-layer model (g - l). The first column (a, d, g, j) shows the "healthy" conductivity σ_1, the second column (b, e, h, k) shows the "hemorrhagic stroke" conductivity σ_2 and the third column (c, f, i, l) shows the change in conductivity $\sigma_2 - \sigma_1$ from the "healthy" to the "hemorrhagic stroke" conductivity. The first row (a, b, c) and the third row (g, h, i) show the true conductivities, and the second row (d, e, f) and the fourth row (j, k, l) show the corresponding reconstructed conductivities. Because of large differences in the conductivity values, the true conductivities and the reconstructed conductivities are shown with different colormaps.

The reconstructed images of the "healthy" and the "hemorrhagic stroke" conductivity distributions are visually identical for both data from the three-layer model (d and e) and the data from the six-layer (j and k) model. In both cases, the reconstructed images of the "hemorrhagic stroke" conductivity distribution alone fail to show an indication of the added perturbation. However, the subtraction images (f) and (l) both indicate the "hemorrhagic stroke" correctly. Of note is the fact that the three-layer model indicates the "hemorrhagic stroke" with better contrast even though the true contrast in conductivity is smaller in the three-layer model (c) than in the six-layer model (i) with the respect of surrounding tissue. This shows that it is easier to monitor the progression of "hemorrhagic stroke" from the data simulated with the three-layer model than from data simulated with the six-layer model. This further implies that using measurement data simulated with the three-layer model might give misleadingly good results and that the six-layer model, or some such more realistic model, should be used for data simulation when the feasibility of EIT for stroke monitoring is evaluated.

IV. Discussion

A. *Assessment of the lead field and sensitivity visualization*

The differences in the electrical conductivity of tissues influence the lead fields. As presented in Fig. 3-6, the sensitivity distribution of the EIT measurement changes significantly depending on the tissues present in the measured volume. The complex geometries of well conductive CSF and relatively poorly conductive white and grey matter in the cranial cavity alter the lead fields and thus the EIT sensitivity distribution considerably. This can be seen when the six-layer model is compared to the three-layer relatively homogenous head model, e.g., in Fig. 3-6. In both three- and six-layer models, the skull reduces the sensitivity inside the cranial cavity compared to the scalp layer. In general, our three-layer model produces similar sensitivity distributions to the simple homogeneous 2D model used by Kauppinen et al. in their study visualizing various current injection patterns [5].

However, in addition to the skull and the scalp also the cranial cavity inhomogeneities are of importance. For example, it can be seen from Fig. 3 in the three-layer tissue model; the

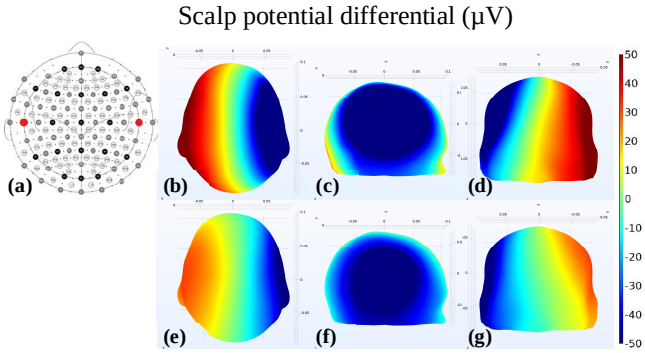

Fig. 10. Difference in scalp potential with and without and perturbation with 8-27 current injection electrodes. (a) current injection electrodes shown in 10-5 map. Six-layer model is on the top row with axial (b), sagittal (c) and coronal (d) views. Three-layer is on the bottom row with axial (e), sagittal (f) and coronal (g) views. It can be seen how the three- and six-layer models produce different results in the scalp potentials when same perturbation is added to both models.

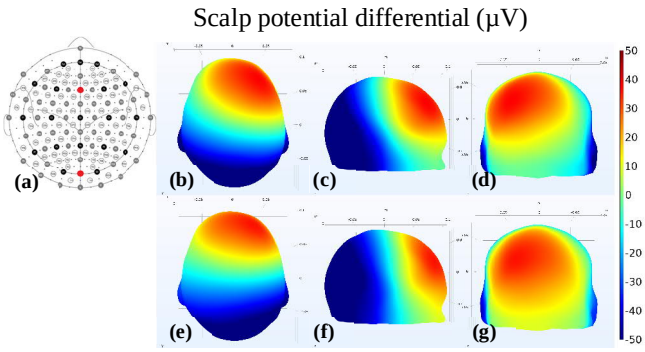

Fig. 11. Difference in scalp potential with and without and perturbation with 1-17 current injection electrodes. (a) current injection electrodes shown in 10-5 map. Six-layer model is on the top row with axial (b), sagittal (c) and coronal (d) views. Three-layer is on the bottom row with axial (e), sagittal (f) and coronal (g) views. The difference between three- and six-layer models is not as large as in Fig. 7 with this current injection electrode pair.

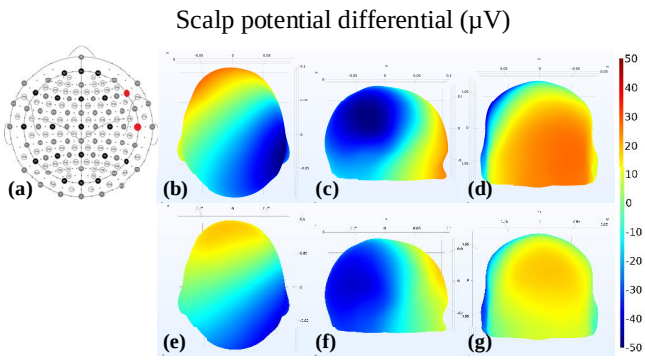

Fig. 12. Difference in scalp potential with and without and perturbation with 8-13 current injection electrodes. (a) current injection electrodes shown in 10-5 map. Six-layer model is on the top row with axial (b), sagittal (c) and coronal (d) views. Three-layer is on the bottom row with axial (e), sagittal (f) and coronal (g) views. With this current injection the perturbation produces the smallest changes in the scalp potentials because the electrodes are close to each other and most of the current is shunted through the scalp and very little enters the cranial cavity. Still, the three- and six-layer models produce different results.

This article has been accepted for publication in a future issue of this journal, but has not been fully edited. Content may change prior to final publication. Citation information: DOI 10.1109/TBME.2021.3120929, IEEE Transactions on Biomedical Engineering

lead field lines are quite evenly distributed. On the other hand, in the six-layer model, the current inside the cranial cavity follows the well-conducting CSF, and the lead field lines are aligned along with the CSF domain or close to it. Also, the difference in the behavior of the lead fields between the three- and six-layer models results in very different sensitivity distributions inside the cranial cavity.

Fig. 6 demonstrates the same effect with two additional current injection and measurement patterns. This implies that the three- and six-layer models will produce different measurement results with the same type of perturbation regardless of the measurement configuration. The same effect is also visible in Fig. 4, which displays the sensitivity distribution of one measurement and injection pair in 3D space. The effect of the CSF is apparent but also sometimes drastically different. The CSF can either improve or decrease the perturbation detection depending on the perturbation location and the electrode configuration used, as shown in Fig. 5-7.

In a model with the perturbation located deeper in the brain (Fig. 6), the sensitivity in the perturbation volume is reduced in the six-layer model compared to the three-layer model. This is caused by the combination of CSF conducting electrical current very well and the brain tissue functioning as an insulator around the perturbation.

When moving the perturbation towards the temporal region (Fig. 5), the sensitivity in the perturbation region improves in the six-layer model as the perturbation gets closer to the CSF, which shunts the current.

In the six-layer model, the same current shunting behavior was observed as in the 3D model used by Seoane et al. [17], even if their results were determined based on two-electrode impedance measurements impractical in actual patient EIT.

All the lead field and sensitivity distribution visualizations lead to the same conclusions; there is a significant difference between the three- and six-layer models. A perturbation also causes a change in the sensitivity distribution inside the cranial cavity compared to a model without a perturbation. In general, this change is much smaller than the change adding CSF on EIT forward simulation.

B. Effect of the perturbation and the model details on the EIT measurement and reconstruction

The effect of the depth and size of the perturbation on the simulated EIT electrode voltages is also considerable. When the perturbation is small and deep in the brain (Fig. 8), the median effect on the EIT measurement is very small. For example, with the small 10 mm hemorrhagic perturbation added into the model, the changes in the median simulated differential voltages generated by the realistic 1 mA current are less than 1 µV. This is just 0.01 % of the simulated differential voltage in both three- and six-layer models and thus below the limit of the detection capabilities with the realistic instrumentation currently available when using scalp electrodes [38].

The relative conductivity change caused by the perturbation with respect to the surrounding tissue in the six-layer model was much larger than in the three-layer model. In the six-layer model, the perturbation with the conductivity of the blood replaced white matter, which had less than one-tenth of the electrical conductivity. In the three-layer model, the blood had only twice the conductivity of the cranial cavity's tissues, but it still produced a similar change in the measured potentials. The sensitivity distributions in Fig. 3-6 further explain these results, as it's visible that the three-layer model provides higher sensitivity in the perturbation region. So, the relatively smaller conductivity change in the three-layer model can produce a similar magnitude of voltage differences as measured from the six-layer model. This is also visible in the reconstruction example provided in the paper, as the reconstructed conductivity change utilizing the data from the three-layer model has better contrast than in the conductivity change obtained from the data of the six-layer model, even if, in reality, the conductivity change contrast was much larger in the six-layer model. This indicates that the three-layer model might not be optimal for assessing the capabilities of new inverse methods.

The potential distributions on the scalp differ between the three- and six-layer models, as seen in Fig. 10-12. As seen in lead field visualization, the CSF shunts the current to cortical regions. Depending on the perturbation location, the CSF may increase or decrease the sensitivity and recorded potentials (Fig. 7). For example, CSF increased the impact of the perturbations closer to the surface of the skull on simulated scalp electrode potentials, leading to higher voltage differences in the six-layer model than in the three-layer model for the perturbations closer to the surface.

Our results imply that if a forward model is used to determine the optimal measurement patterns, it is important to have accurate anatomical structures, including CSF in the model. There are notable potential differences between the simplified three-layer model and the more anatomically realistic six-layer model with some current injection patterns (Fig. 9). For example, the 30 mm perturbation deep in the brain, 65 mm from the surface of the scalp, causes approximately 0.30 % change in the simulated differential potentials (Fig. 7). The difference between the three- and six-layer models with the same perturbation is 4.6 %. Our results show that the modeling error when using a three-layer model is an order of magnitude larger than the potential differences emerging from the perturbations. Thus, the voltage simulation results manifest the importance of the accurate anatomical details of the CSF and brain in modeling the EIT measurements.

In general, the effect of the frequency on the detected voltages was small within the frequency range used in our simulations. The low frequencies exhibited marginally larger percentual changes; however, the differences were minor. Also, the lead fields were practically unaltered, so all lead field visualizations are only shown at 100 kHz frequency.

C. Considerations for computational and anatomical phantoms

Our results show a significant difference between the three- and six-layer models when it comes to how sensitive the EIT measurement is to the perturbation. Based on these results, using high-fidelity computational forward models would be ideal when testing stroke EIT algorithms. Even with the robust time-difference methods, the highly conductive CSF layer can

mask the true conductivity change caused by the perturbation and thus make monitoring of progression of ICH more difficult.

Currently, most of the research with water tank-type phantoms is limited to three-layer phantoms. However, modern manufacturing techniques employing 3D printing and casting have been used for transcranial direct current stimulation [39] and EIT [40] phantoms with high-fidelity anatomical details. The 3D printable conductive polymers enable the preservation of details of the brain. The use of high-fidelity phantoms with detailed anatomical features beyond the three-layer model should be more widely considered in the EIT community. Manufacturing of high-fidelity phantoms is more labor-intensive than using the traditional three-layer phantoms, so the computational in silico models presented in this paper could be used to determine what type of simplifications are justifiable for EIT phantoms.

D. Limitations and strengths of chosen methods

This study concentrated mainly on the effect of accurate tissue geometries inside the cranial cavity on the simulated EIT measurements. Simplified models produce significantly different results than the anatomically more realistic models, where the presence of the CSF can partially mask the effect of a hemorrhagic lesion, as shown by the sensitivity distributions and the reconstruction examples. The lead field approach and the analysis of the simulated EIT voltages provide a powerful way to visualize and quantify the effects of the model errors and the detectability of the stroke perturbations.

While the complete electrode model was used to model the scalp electrodes, it was not configured with frequency-dependent complex impedance for the electrodes. Additionally, despite being frequency-dependent, the material properties in our simulation were considered isotropic. Skull and white matter are anisotropic, but this is usually omitted in EIT studies [18]. The scalp was modeled as a single layer, and the skull was a closed skull model. Further, we used spherical perturbations instead of realistically shaped ones. However, these limitations do not affect our modeling results' main conclusions, highlighting the need for accurate geometries and material properties, especially regarding the CSF on EIT forward and inverse estimation.

V. Conclusions

Our results highlight that the effect of the CSF on the EIT measurement for stroke imaging is too significant to be ignored in computational modeling. The high electrical conductivity and the irregular shape of the CSF volume alter the EIT measurement sensitivity distribution and the recorded voltages as seen in comparing the three- and six-layer models.

This highlights the need for accurate modeling when developing EIT stroke monitoring algorithms. This could pose a problem in diagnostics; however, in patient monitoring, using a priori information from the patient CT and MR images to construct a proper a-priori personalized head model could provide the solution for the challenges caused by the complex CSF volume shape.

Our results demonstrate that the lead field concept provides excellent insight into the measurement capabilities. Lead fields can also be used to design optimized measurement strategies for monitoring the progression of a hemorrhagic stroke, especially when CT or MR images are available and the location of the original stroke is known. This would allow determining the current injection and measurement patterns that provide the best sensitivity for that region of the brain. However, our results showcase that correct anatomical details of the forward model are needed for assessing the EIT measurement and the fidelity of the inverse methods.

Overall, our study aims to clarify the need for accurate head models for EIT-based stroke monitoring. Based on our results, we can conclude that perhaps one of the possible reasons the previous clinical study [12] on stroke classification ended up with negative findings is the use of simplified geometries for both the forward model for finding the most sensitive measurement patterns and the inverse model for reconstructing the EIT images.

References

[1] E. S. Donkor, "Stroke in the 21st Century: A Snapshot of the Burden, Epidemiology, and Quality of Life," *Stroke Res. Treat.*, vol. 2018, 2018, doi: 10.1155/2018/3238165.

[2] S. Chen, L. Zeng, and Z. Hu, "Progressing haemorrhagic stroke: categories, causes, mechanisms and managements," *J. Neurol.*, vol. 261, no. 11, pp. 2061–2078, 2014, doi: 10.1007/s00415-014-7291-1.

[3] J. A. Caceres and J. N. Goldstein, "Intracranial Hemorrhage," *Emerg. Med. Clin. North Am.*, vol. 30, no. 3, pp. 771–794, Aug. 2012, doi: 10.1016/J.EMC.2012.06.003.

[4] J. N. Goldstein and A. J. Gilson, "Critical care management of acute intracerebral hemorrhage," *Curr. Treat. Options Neurol.*, vol. 13, no. 2, pp. 204–216, 2011, doi: 10.1007/s11940-010-0109-2.

[5] P. Kauppinen, J. Hyttinen, and J. Malmivuo, "Sensitivity Distribution Visualizations of Impedance Tomography Measurement Strategies," *Int. J. Bioelectromagn.*, vol. 8, no. 1, p. VII/1-VII/9, 2006.

[6] D. S. Holder, "Electrical impedance tomography (EIT) of brain function," *Brain Topogr.*, vol. 5, no. 2, pp. 87–93, 1992.

[7] W. Lionheart, N. Polydorides, and A. Borsic, "The reconstruction problem," *Electr. impedance Tomogr. methods, Hist. Appl.*, vol. 750309520, pp. 3–64, 2005.

[8] A. Witkowska-Wrobel, K. Aristovich, M. Faulkner, J. Avery, and D. Holder, "Feasibility of imaging epileptic seizure onset with EIT and depth electrodes," *Neuroimage*, vol. 173, no. November 2017, pp. 311–321, 2018, doi: 10.1016/j.neuroimage.2018.02.056.

[9] M. Jehl, J. Avery, E. Malone, D. Holder, and T. Betcke, "Correcting electrode modelling errors in EIT on realistic 3D head models," *Physiol. Meas.*, vol. 36, no. 12, pp. 2423–2442, 2015, doi: 10.1088/0967-

3334/36/12/2423.

[10] E. Malone, M. Jehl, S. Arridge, T. Betcke, and D. Holder, "Stroke type differentiation using spectrally constrained multifrequency EIT: Evaluation of feasibility in a realistic head model," *Physiol. Meas.*, vol. 35, no. 6, pp. 1051–1066, 2014, doi: 10.1088/0967-3334/35/6/1051.

[11] J. Toivanen, A. Hänninen, T. Savolainen, N. Forss, and V. Kolehmainen, "Monitoring hemorrhagic strokes using EIT," in *Bioimpedance and Spectroscopy*, Elsevier, 2021, pp. 271–298.

[12] A. Romsauerova, A. McEwan, L. Horesh, R. Yerworth, R. H. Bayford, and D. S. Holder, "Multi-frequency electrical impedance tomography (EIT) of the adult human head: Initial findings in brain tumours, arteriovenous malformations and chronic stroke, development of an analysis method and calibration," *Physiol. Meas.*, vol. 27, no. 5, 2006, doi: 10.1088/0967-3334/27/5/S13.

[13] D. B. Geselowitz, "An Application of Electrocardiographic Lead Theory to Impedance Plethysmography," *IEEE Trans. Biomed. Eng.*, vol. BME-18, no. 1, pp. 38–41, 1971, doi: 10.1109/TBME.1971.4502787.

[14] J. Malmivuo, R. Plonsey, and others, *Bioelectromagnetism: principles and applications of bioelectric and biomagnetic fields.* Oxford University Press, USA, 1995.

[15] P. K. Kauppinen, J. A. Hyttinen, and J. A. Malmivuo, "Sensitivity distributions of impedance cardiography using band and spot electrodes analyzed by a three-dimensional computer model," *Ann. Biomed. Eng.*, vol. 26, no. 4, pp. 694–702, 1998, doi: 10.1114/1.44.

[16] M. Böttrich, J. M. A. Tanskanen, and J. A. K. Hyttinen, "Lead field theory provides a powerful tool for designing microelectrode array impedance measurements for biological cell detection and observation," *Biomed. Eng. Online*, vol. 16, no. 1, pp. 1–17, 2017, doi: 10.1186/s12938-017-0372-5.

[17] F. Seoane, M. Lu, M. Persson, and K. Lindecrantz, "Electrical bioimpedance cerebral monitoring. A study of the current density distribution and impedance sensitivity maps on a 3D realistic head model," *Proc. 3rd Int. IEEE EMBS Conf. Neural Eng.*, pp. 256–260, 2007, doi: 10.1109/CNE.2007.369660.

[18] J. F. P. J. Abascal *et al.*, "Use of anisotropic modelling in electrical impedance tomography; Description of method and preliminary assessment of utility in imaging brain function in the adult human head," *Neuroimage*, vol. 43, no. 2, pp. 258–268, 2008, doi: 10.1016/j.neuroimage.2008.07.023.

[19] H. Li *et al.*, "Unveiling the development of intracranial injury using dynamic brain EIT: An evaluation of current reconstruction algorithms," *Physiol. Meas.*, vol. 38, no. 9, pp. 1776–1790, 2017, doi: 10.1088/1361-6579/aa8016.

[20] A. Tizzard, L. Horesh, R. J. Yerworth, D. S. Holder, and R. H. Bayford, "Generating accurate finite element meshes for the forward model of the human head in EIT," in *Physiological Measurement*, 2005, vol. 26, no. 2, doi: 10.1088/0967-3334/26/2/024.

[21] M. Vonach *et al.*, "A method for rapid production of subject specific finite element meshes for electrical impedance tomography of the human head," *Physiol. Meas.*, vol. 33, no. 5, pp. 801–816, 2012, doi: 10.1088/0967-3334/33/5/801.

[22] B. McDermott, J. Avery, M. O'Halloran, K. Aristovich, and E. Porter, "Bi-frequency symmetry difference electrical impedance tomography- A novel technique for perturbation detection in static scenes," *Physiol. Meas.*, vol. 40, no. 4, 2019, doi: 10.1088/1361-6579/ab08ba.

[23] Q. He, A. Rezaei, and S. Pursiainen, "Zeffiro User Interface for Electromagnetic Brain Imaging: a GPU Accelerated FEM Tool for Forward and Inverse Computations in Matlab," *Neuroinformatics*, 2019, doi: 10.1007/s12021-019-09436-9.

[24] J. Avery, K. Aristovich, B. Low, and D. Holder, "Reproducible 3D printed head tanks for electrical impedance tomography with realistic shape and conductivity distribution," *Physiol. Meas.*, vol. 38, no. 6, pp. 1116–1131, 2017, doi: 10.1088/1361-6579/aa6586.

[25] J. Li *et al.*, "A New Head Phantom With Realistic Shape and Spatially Varying Skull Resistivity Distribution," vol. 61, no. 2, pp. 254–263, 2014.

[26] S. Ahn, T. I. Oh, S. C. Jun, J. K. Seo, and E. J. Woo, "Validation of weighted frequency-difference EIT using a three-dimensional hemisphere model and phantom," *Physiol. Meas.*, vol. 32, no. 10, p. 1663, 2011, doi: 10.1088/0967-3334/32/10/013.

[27] B. Packham *et al.*, "Comparison of frequency difference reconstruction algorithms for the detection of acute stroke using EIT in a realistic head-shaped tank," *Physiol. Meas.*, vol. 33, no. 5, p. 767, 2012, doi: 10.1088/0967-3334/33/5/767.

[28] M. Jehl, K. Aristovich, M. Faulkner, and D. Holder, "Are patient specific meshes required for EIT head imaging?," *Physiol. Meas.*, vol. 37, no. 6, pp. 879–892, 2016, doi: 10.1088/0967-3334/37/6/879.

[29] E. G. Lee, R. L. Hadimani, and D. C. Jiles, "Population Head Model Repository V1. 0," *IT'IS Found. Switz.*, 2016.

[30] N. Goren *et al.*, "Data Descriptor: Multi-frequency electrical impedance tomography and neuroimaging data in stroke patients," *Sci. Data*, vol. 5, pp. 1–10, 2018, doi: 10.1038/sdata.2018.112.

[31] C. Gabriel, S. Gabriel, and E. Corthout, "The dielectric properties of biological tissues: III. Parametric models for the dielectric spectrum of tissues," *Phys. Med. Biol.*, vol. 41, no. 11, pp. 2271–2294, 1996, [Online]. Available: http://iopscience.iop.org/article/10.1088/0031-9155/41/11/003/pdf.

[32] N. Hyvönen and L. Mustonen, "Smoothened Complete Electrode Model," *SIAM J. Appl. Math.*, vol. 77, no. 6, pp. 2250–2271, 2017, doi: 10.1137/17m1124292.

[33] A. Fouchard, S. Bonnet, L. Hervé, and O. David, "Flexible Numerical Platform for Electrical

Impedance Tomography," *Comsol Conf.*, pp. 1–7, 2015, doi: 10.2298/VSP1302221B.

[34] J. Górecka and P. Makiewicz, "The dependence of electrode impedance on the number of performed eeg examinations," *Sensors (Switzerland)*, vol. 19, no. 11, 2019, doi: 10.3390/s19112608.

[35] S. Russo, S. Nefti-Meziani, N. Carbonaro, and A. Tognetti, "Development of a High-Speed Current Injection and Voltage Measurement System for Electrical Impedance Tomography-Based Stretchable Sensors," *Technologies*, vol. 5, no. 3, p. 48, 2017, doi: 10.3390/technologies5030048.

[36] G. González, V. Kolehmainen, and A. Seppänen, "Isotropic and anisotropic total variation regularization in electrical impedance tomography," *Comput. Math. with Appl.*, vol. 74, no. 3, pp. 564–576, 2017, doi: 10.1016/j.camwa.2017.05.004.

[37] L. I. Rudin, S. Osher, and E. Fatemi, "Nonlinear total variation based noise removal algorithms," *Phys. D nonlinear Phenom.*, vol. 60, no. 1–4, pp. 259–268, 1992.

[38] J. Avery, T. Dowrick, M. Faulkner, N. Goren, and D. Holder, "A versatile and reproducible multi-frequency electrical impedance tomography system," *Sensors (Switzerland)*, vol. 17, no. 2, 2017, doi: 10.3390/s17020280.

[39] L. Morales-Quezada, M. M. El-Hagrassy, B. Costa, R. A. McKinley, P. Lv, and F. Fregni, "Transcranial Direct Current Stimulation Optimization – From Physics-Based Computer Simulations to High-Fidelity Head Phantom Fabrication and Measurements," *Front. Hum. Neurosci.*, vol. 13, no. October, pp. 1–15, 2019, doi: 10.3389/fnhum.2019.00388.

[40] J. Zhang *et al.*, "A novel 3D-printed head phantom with anatomically realistic geometry and continuously varying skull resistivity distribution for electrical impedance tomography," *Sci. Rep.*, vol. 7, no. 1, pp. 1–9, 2017, doi: 10.1038/s41598-017-05006-8.